

A discontinuous Galerkin scheme for elliptic equations on extremely stretched grids

Nils L. Vu ^{1, *}

¹*Theoretical Astrophysics, Walter Burke Institute for Theoretical Physics,
California Institute of Technology, Pasadena, California 91125, USA*

(Dated: May 13, 2024)

Discontinuous Galerkin (DG) methods for solving elliptic equations are gaining popularity in the computational physics community for their high-order spectral convergence and their potential for parallelization on computing clusters. However, problems in numerical relativity with extremely stretched grids, such as initial data problems for binary black holes that impose boundary conditions at large distances from the black holes, have proven challenging for DG methods. To alleviate this problem we have developed a primal DG scheme that is generically applicable to a large class of elliptic equations, including problems on curved and extremely stretched grids. The DG scheme accommodates two widely used initial data formulations in numerical relativity, namely the puncture formulation and the extended conformal thin-sandwich (XCTS) formulation. We find that our DG scheme is able to stretch the grid by a factor of $\sim 10^9$ and hence allows to impose boundary conditions at large distances. The scheme converges exponentially with resolution both for the smooth XCTS problem and for the non-smooth puncture problem. With this method we are able to generate high-quality initial data for binary black hole problems using a parallelizable DG scheme. The code is publicly available in the open-source `SpECTRE` numerical relativity code.

I. INTRODUCTION

Discontinuous Galerkin (DG) methods are a class of spectral finite-element numerical methods for solving partial differential equations (PDEs). Although most prevalently applied to hyperbolic conservation laws, DG methods can also be advantageous for elliptic equations [1, 2]. Their spectral elements are able to retain exponential convergence rates [3], and the domain decomposition allows for efficient parallelization on large computing clusters [4, 5]. However, DG methods can be complicated to implement, which is why people often choose finite-difference or finite-volume methods despite the advantages of DG methods.

Furthermore, problems in the field of numerical relativity often involve extremely stretched grids to impose boundary conditions at very large distances, which can be challenging for DG methods. Specifically, initial data problems in general relativity with black holes or neutron stars are typically solved on spherical domains centered on the objects. Since the solution at the outer boundary of the sphere is unknown but typically falls off as $1/r$ with coordinate distance from the center, the boundary condition is set to empty flat spacetime at a large but finite radius R ("approximate asymptotic flatness") [6]. This approach incurs an error of $\mathcal{O}(1/R)$ on the solution, which is reduced below numerical accuracy by pushing the outer boundary far enough out, often to $R \sim 10^9$. To resolve this large computational volume numerically, radial grid points are also distributed on a $1/r$ scale. This way, a large spherical shell can be resolved by just a few spectral elements that are extremely stretched. While this

strategy has worked well for specialized spectral numerical schemes in the past [6], generic DG schemes struggle with the extremely large Jacobian factors that arise from the grid stretching. In this article we construct a weak primal DG scheme for generic elliptic equations that is capable of handling extreme grid stretching. The scheme is implemented in the open-source numerical relativity code `SpECTRE` [7].

To further alleviate the strain that the extreme grid stretching can pose on the numerical scheme, we propose new Robin-type boundary conditions at the outer boundary. These boundary conditions incur an error of only $\mathcal{O}(1/R^2)$, so the outer boundary can be placed at a smaller radius, $R \sim 10^5$, while still maintaining the same level of error. To this end, we develop new Robin-type boundary conditions for the extended conformal thin sandwich (XCTS) formulation of the Einstein constraint equations.

Alternative approaches to the extreme grid stretching have been proposed on the level of the elliptic equations themselves. For example, the `LORENE` [8, 9], `KADATH` [10, 11], and `SGRID` [12] libraries employ multiple computational domains and a radial coordinate transformation to compactify the outermost domain. This allows to impose boundary conditions at spatial infinity rather than at a finite radius, but requires special treatment of derivative operators in the different domains to incorporate the coordinate transformation. The `TwoPunctures` code [13] employs a similar compactification on a single domain, rewriting the elliptic equations in compactified coordinates. With the numerical scheme developed in this article we can avoid such special coordinate transformations, leading to a more flexible scheme.

This article is structured as follows. Section II formulates the weak primal DG scheme for generic elliptic equations. Section III demonstrates the versatility of

* nilsvu@caltech.edu

the DG scheme by solving a simple Poisson problem and two classic general-relativistic initial data problems with black holes on extremely stretched grids. We conclude in Section IV.

II. DISCONTINUOUS GALERKIN FORMULATION

The discontinuous Galerkin (DG) formulation developed here applies to any set of coupled, nonlinear elliptic equations that can be written in first-order flux form,

$$-\partial_i \mathcal{F}_\alpha^i [u, \partial u; \mathbf{x}] + \mathcal{S}_\alpha [u, \partial u; \mathbf{x}] = f_\alpha(\mathbf{x}), \quad (1)$$

where \mathcal{F}_α^i are the fluxes, \mathcal{S}_α are the sources, and f_α are the fixed sources. The index α enumerates the set of equations and variables. The fluxes and sources are functionals of the variables $u_\alpha(\mathbf{x})$ and their first derivatives. The fluxes \mathcal{F}_α^i must be linear in the variables and their derivatives, which means they can be written in the form

$$\mathcal{F}_\alpha^i = \mathcal{A}_{\alpha\beta}^{ij} \partial_j u_\beta + \mathcal{B}_{\alpha\beta}^i u_\beta. \quad (2)$$

The sources \mathcal{S}_α can be nonlinear. The fixed sources $f_\alpha(\mathbf{x})$ are independent of the variables. They can be absorbed in the sources \mathcal{S}_α , but are kept separate here because their constant contribution to the sources introduces a nonlinearity into otherwise linear equations [5]. Equation (1) closely resembles formulations of hyperbolic conservation laws but allows the fluxes \mathcal{F}_α^i to be higher-rank tensor fields. It is a simplification of the first-order flux form defined in Ref. [5] that arises by selecting the gradients of the variables as first-order auxiliary variables.

For example, a Poisson equation for the variable $u(\mathbf{x})$ on a curved manifold with metric $g_{ij}(\mathbf{x})$ in Cartesian coordinates is

$$-g^{ij} \nabla_i \nabla_j u(\mathbf{x}) = f(\mathbf{x}), \quad (3)$$

where ∇_i is the covariant derivative compatible with the metric g_{ij} . It can be written in first-order flux form (1) with the fluxes and sources

$$\mathcal{F}^i = g^{ij} \partial_j u, \quad \mathcal{S} = -\Gamma_{ij}^i \mathcal{F}^j, \quad (4a)$$

where $\Gamma_{jk}^i = \frac{1}{2} g^{il} (\partial_j g_{kl} + \partial_k g_{jl} - \partial_l g_{jk})$ are the Christoffel symbols associated with the metric g_{ij} . Any Poisson equation with nonlinear sources, such as the puncture equation solved in Section III B for simple binary black hole initial data, can be written in this form as well.

Also the extended conformal thin-sandwich (XCTS) formulation of the Einstein constraint equations [14–16], that we solve for binary black hole initial data in Section III C, can be written in first-order flux form (1). The XCTS equations are a set of five coupled, nonlinear elliptic

equations for the variables $\{\psi, \alpha\psi, \beta^i\}$ given by

$$\bar{\nabla}^2 \psi = \frac{1}{8} \psi \bar{R} + \frac{1}{12} \psi^5 K^2 \quad (5a)$$

$$- \frac{1}{8} \psi^{-7} \bar{A}_{ij} \bar{A}^{ij} - 2\pi \psi^5 \rho$$

$$\begin{aligned} \bar{\nabla}^2 (\alpha\psi) = \alpha\psi \left(\frac{7}{8} \psi^{-8} \bar{A}_{ij} \bar{A}^{ij} + \frac{5}{12} \psi^4 K^2 + \frac{1}{8} \bar{R} \right. \\ \left. + 2\pi \psi^4 (\rho + 2S) \right) - \psi^5 \partial_t K + \psi^5 \beta^i \bar{\nabla}_i K \end{aligned} \quad (5b)$$

$$\begin{aligned} \bar{\nabla}_i (\bar{L}\beta)^{ij} = (\bar{L}\beta)^{ij} \bar{\nabla}_i \ln(\bar{\alpha}) + \bar{\alpha} \bar{\nabla}_i (\bar{\alpha}^{-1} \bar{u}^{ij}) \\ + \frac{4}{3} \bar{\alpha} \psi^6 \bar{\nabla}^j K + 16\pi \bar{\alpha} \psi^{10} S^j \end{aligned} \quad (5c)$$

with $\bar{A}^{ij} = \frac{1}{2\bar{\alpha}} ((\bar{L}\beta)^{ij} - \bar{u}^{ij})$ and $\bar{\alpha} = \alpha\psi^{-6}$. The XCTS equations are formulated on a background geometry defined by the conformal metric $\bar{\gamma}_{ij}$, which also defines the covariant derivative $\bar{\nabla}$, the Ricci scalar \bar{R} , and the longitudinal operator

$$(\bar{L}\beta)^{ij} = \bar{\nabla}^i \beta^j + \bar{\nabla}^j \beta^i - \frac{2}{3} \bar{\gamma}^{ij} \bar{\nabla}_k \beta^k. \quad (6)$$

The conformal metric is chosen in advance alongside the trace of the extrinsic curvature K , their respective time derivatives \bar{u}_{ij} and $\partial_t K$, and the matter sources ρ , S , and S^i . Appendix A lists the fluxes and sources to formulate the XCTS equations in first-order flux form (1).

Therefore, a generic implementation of the DG discretization for the first-order flux form (1) encompasses a large class of elliptic equations, including the puncture and XCTS initial data formulations for black holes. It also encompasses other (nonlinear) Poisson-type equations, as well as linear elasticity [17]. The versatility of this generic formulation lowers the barrier of entry for using the DG method in our code, since new equations can be added by implementing their fluxes and sources without having to learn the details of the DG discretization scheme. In the following we will derive the DG discretization scheme without reference to any specific elliptic equations.

A. Domain decomposition

To formulate the DG scheme we decompose the computational domain Ω into deformed cubes, called elements Ω_k , as described in more detail in Refs. [4, 5]. In this article we focus on extremely stretched wedge-shaped elements as pictured in Fig. 1 from which we build spherical domains.

To deform the hexahedral elements to wedges we employ an invertible map from *logical* coordinates $\boldsymbol{\xi} = (\xi, \eta, \zeta) \in [-1, 1]^3$ on the reference cube to the coordinates $\mathbf{x} \in \Omega_k$ in which the elliptic equations (1) are formulated. The coordinate map also defines the Jacobian matrix

$$J_j^i := \frac{\partial x^i}{\partial \xi^j} \quad (7)$$

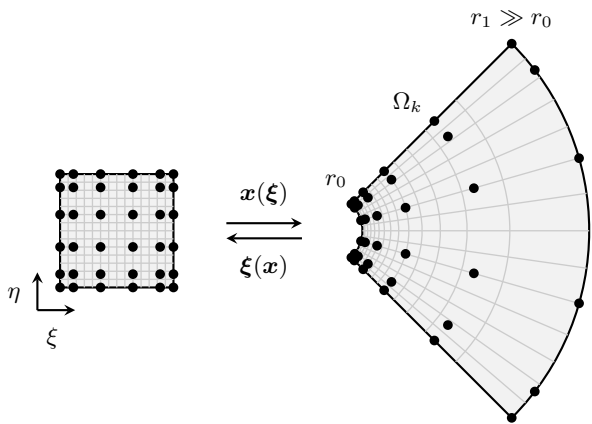


FIG. 1. Geometry of an extremely stretched wedge-shaped element Ω_k in two dimensions. The coordinate transformation $\mathbf{x}(\boldsymbol{\xi})$ deforms a reference cube $\boldsymbol{\xi} \in [-1, 1]^2$ to a wedge with inner radius r_0 and outer radius $r_1 \gg r_0$. Coordinates are mapped with an $1/r$ inverse radial scaling, as illustrated by the light gray lines. Grid points are chosen as Legendre-Gauss-Lobatto collocation points on the reference cube (black dots).

with determinant J and inverse $(J^{-1})_i^j = \partial \xi^j / \partial x^i$. The wedge coordinate map pictured in Fig. 1 is

$$\mathbf{x}(\boldsymbol{\xi}) = \frac{r(\xi)}{\sqrt{1 + \eta^2 + \zeta^2}} \begin{pmatrix} 1 \\ \eta \\ \zeta \end{pmatrix} \quad (8)$$

in three dimensions, where $r(\xi)$ is the radial coordinate mapping. We choose either a linear, logarithmic, or inverse radial mapping,

$$\text{linear} \quad r(\xi) = \frac{1}{2} ((1 - \xi)r_0 + (1 + \xi)r_1) \quad (9a)$$

$$\text{logarithmic} \quad \ln r(\xi) = \frac{1}{2} ((1 - \xi) \ln r_0 + (1 + \xi) \ln r_1) \quad (9b)$$

$$\text{inverse} \quad \frac{1}{r(\xi)} = \frac{1}{2} \left(\frac{1 - \xi}{r_0} + \frac{1 + \xi}{r_1} \right). \quad (9c)$$

Here, r_0 and r_1 denote the inner and outer radii of the wedge.

For illustration, we can quantify how much the reference cube is stretched by the wedge map with the inverse radial mapping, Eq. (9c). First, note that the midpoint of the reference cube, $\xi = 0$, is mapped to only $r_{\text{mid}} = 2r_0$ in the limit $r_1 \gg r_0$. Second, the Jacobian determinant at the outer radius is $J \propto (r_1)^4 / r_0$ in the limit $r_1 \gg r_0$. This means that for $r_0 = 10$ and $r_1 = 10^9$ the midpoint is mapped to only $r_{\text{mid}} \sim 20$ and the Jacobian determinant is $J \sim 10^{35}$. Our DG scheme has to be able to handle such extreme stretching.

For the DG discretization we choose a regular grid of $N_k = \prod_{i=1}^3 N_{k,i}$ Legendre-Gauss-Lobatto (LGL) collocation points $\boldsymbol{\xi}_p = (\xi_{p1}, \eta_{p2}, \zeta_{p3})$ on the reference cube of element Ω_k , as illustrated in Fig. 1 and described in

more detail in Ref. [5]. Fields on the computational domain are represented by their values at these grid points. This nodal representation is facilitated by expanding each component $u(\mathbf{x})$ as

$$u(\mathbf{x}) = \sum_p^{N_k} u_p \psi_p(\boldsymbol{\xi}(\mathbf{x})). \quad (10)$$

Here, $u_p = u(\mathbf{x}(\boldsymbol{\xi}_p))$ are the nodal coefficients and $\psi_p(\boldsymbol{\xi})$ are the basis functions

$$\psi_p(\boldsymbol{\xi}) = \prod_{i=1}^3 \ell_{p_i}(\xi^i), \quad (11)$$

which are products of the one-dimensional Lagrange interpolating polynomials $\ell_{p_i}(\xi)$ with respect to the LGL collocation points $\boldsymbol{\xi}_p$ on the reference cube. Note that Legendre-Gauss grids (where no grid point is placed on the element boundary) were unable to handle the extreme grid stretching with the DG schemes we tested.

B. DG residuals

To derive the primal DG formulation for the elliptic equations, we project the flux form, Eq. (1), on the set of basis functions ψ_p to obtain the DG residuals

$$-(\psi_p, \partial_i \mathcal{F}^i)_{\Omega_k} + (\psi_p, \mathcal{S})_{\Omega_k} = (\psi_p, f)_{\Omega_k}, \quad (12)$$

where the inner product is defined as

$$(\phi, \pi)_{\Omega_k} := \int_{\Omega_k} \phi(\mathbf{x}) \pi(\mathbf{x}) \sqrt{g} d^3x \quad (13a)$$

$$= \int_{[-1,1]^3} \phi(\mathbf{x}(\boldsymbol{\xi})) \pi(\mathbf{x}(\boldsymbol{\xi})) \sqrt{g} J d^3\xi. \quad (13b)$$

Here, g is the determinant of the metric g_{ij} that covariant derivatives in the equations are compatible with. For the XCTS equations, this is the conformal metric $\tilde{\gamma}_{ij}$. We suppress the index α that enumerates equations and variables in this section.

A partial integration of Eq. (12) gives the weak form of the DG residuals,

$$(\partial_i \psi_p, \mathcal{F}^i)_{\Omega_k} - (\psi_p, (n_i \mathcal{F}^i)^*)_{\partial \Omega_k} + (\psi_p, \mathcal{S})_{\Omega_k} = (\psi_p, f)_{\Omega_k}, \quad (14)$$

where the inner product on the element boundary is defined as

$$(\phi, \pi)_{\partial \Omega_k} := \int_{\partial \Omega_k} \phi(\mathbf{x}) \pi(\mathbf{x}) \sqrt{g^\Sigma} d^2x \quad (15a)$$

$$= \int_{[-1,1]^2} \phi(\mathbf{x}(\boldsymbol{\xi})) \pi(\mathbf{x}(\boldsymbol{\xi})) \sqrt{g^\Sigma} J^\Sigma d^2\xi \quad (15b)$$

with the surface metric determinant g^Σ induced by the metric g_{ij} and the surface Jacobian J^Σ . We have also introduced the numerical fluxes $(n_i \mathcal{F}^i)^*$ on element boundaries

in Eq. (14), which couple the DG residuals on neighboring elements as discussed in Section II C.

Now, to discretize the auxiliary first-order equation for the fluxes \mathcal{F}^i we employ a primal formulation rather than the Schur-complement approach used in Ref. [5]. This is because the Schur-complement approach, while simpler to implement, fails to handle extremely stretched grids. The two approaches differ only in the boundary correction term arising from the auxiliary equation for the fluxes \mathcal{F}^i . We project the linear decomposition of the fluxes, Eq. (2), on the derivatives of the basis functions to find an expression for the first term in Eq. (14), and integrate by parts, to obtain

$$\begin{aligned} (\partial_i \psi_p, \mathcal{F}^i)_{\Omega_k} &= (\partial_i \psi_p, \mathcal{A}^{ij} \partial_j u)_{\Omega_k} + (\partial_i \psi_p, \mathcal{B}^i u)_{\Omega_k} \quad (16a) \\ &= -(\partial_j \mathcal{A}^{ij} \partial_i \psi_p, u)_{\Omega_k} + (\partial_i \psi_p, \mathcal{B}^i u)_{\Omega_k} \\ &\quad + (\partial_i \psi_p, \mathcal{A}^{ij} n_j u^*)_{\partial \Omega_k}, \end{aligned} \quad (16b)$$

where u^* is the auxiliary numerical flux discussed in Section II C. With another partial integration we find

$$\begin{aligned} (\partial_i \psi_p, \mathcal{F}^i)_{\Omega_k} &= (\partial_i \psi_p, \mathcal{A}^{ij} \partial_j u)_{\Omega_k} + (\partial_i \psi_p, \mathcal{B}^i u)_{\Omega_k} \quad (17a) \\ &\quad + (\partial_i \psi_p, \mathcal{A}^{ij} n_j (u^* - u))_{\partial \Omega_k} \\ &= (\partial_i \psi_p, \mathcal{F}^i)_{\Omega_k} + (\partial_i \psi_p, \mathcal{A}^{ij} n_j (u^* - u))_{\partial \Omega_k}. \end{aligned} \quad (17b)$$

Inserting this result into Eq. (14) we find the primal DG residuals in weak form,

$$\begin{aligned} (\partial_i \psi_p, \mathcal{F}^i)_{\Omega_k} + (\partial_i \psi_p, \mathcal{A}^{ij} n_j (u^* - u))_{\partial \Omega_k} \\ - (\psi_p, (n_i \mathcal{F}^i)^*)_{\partial \Omega_k} + (\psi_p, \mathcal{S})_{\Omega_k} = (\psi_p, f)_{\Omega_k}, \end{aligned} \quad (18)$$

where u^* and $(n_i \mathcal{F}^i)^*$ are the numerical fluxes discussed in the next section. Written in terms of discrete matrices over the element's grid points, as detailed in Ref. [5], the primal DG residuals in weak form are

$$\begin{aligned} MD_i^T \cdot \mathcal{F}^i + MLD_i^T \cdot \mathcal{A}^{ij} n_j (u^* - u) \\ - ML \cdot (n_i \mathcal{F}^i)^* + M \cdot \mathcal{S} = M \cdot f, \end{aligned} \quad (19)$$

where $\mathcal{F}^i = \mathcal{A}^{ij} (J^{-1})_j^{\hat{j}} D_{\hat{j}} \cdot u + \mathcal{B}^i u$. The symbol \cdot denotes matrix-vector multiplication over grid points, and we have defined the mass matrix and weak stiffness matrix in the volume of the element,

$$M_{pq} = \delta_{pq} \sqrt{g}|_p J|_p \prod_{j=1}^3 w_{p_j}, \quad (20)$$

$$MLD_{i,pq}^T = D_{i,pq}^T \sqrt{g}|_q J|_q (J^{-1})_i^{\hat{i}}|_q \prod_{j=1}^3 w_{q_j}, \quad (21)$$

and the lifting matrices from the element boundary to

the volume of the element,

$$ML_{p\bar{q}} = \delta_{p\bar{q}} \sqrt{g^\Sigma}|_{\bar{q}} J^\Sigma|_{\bar{q}} \prod_{j=1}^2 w_{\bar{q}_j}, \quad (22)$$

$$MLD_{i,p\bar{q}}^T = D_{i,p\bar{q}}^T \sqrt{g^\Sigma}|_{\bar{q}} J^\Sigma|_{\bar{q}} (J^{-1})_i^{\hat{i}}|_{\bar{q}} \prod_{j=1}^2 w_{\bar{q}_j}. \quad (23)$$

Here, we have evaluated the integrals in Eq. (18) over the reference cube using Gauss-Lobatto quadrature. The coefficients w_{p_j} are the Gauss-Lobatto quadrature weights in dimension \hat{j} of the reference cube. The logical differentiation matrix is defined as

$$D_{i,pq} = \ell'_{q_i}(\xi_{p_i}) \prod_{\hat{j} \neq \hat{i}}^3 \delta_{p_j q_j}. \quad (24)$$

It takes the derivative along dimension \hat{i} on the reference cube. Indices with a bar, i.e., \bar{q} , only enumerate grid points on the boundary of the element.

Only the MLD_i^T term in Eq. (19) is different from the Schur-complement approach used in Ref. [5], Eq. (30b). It involves a lifting operation with the weak differentiation matrix and only Jacobians evaluated on the element faces. Furthermore, we use the weak form of the DG residuals rather than the strong form used in Ref. [5]. This has proven essential to handle the extreme grid stretching as well.

C. Generalized internal penalty flux

For the numerical fluxes in the DG residuals (18) we choose the generalized internal penalty flux introduced in Ref. [5]. Using the simplified first-order flux form, Eq. (1), the generalized internal penalty flux is

$$u^* = \frac{1}{2} (u^{\text{int}} + u^{\text{ext}}) \quad (25a)$$

$$\begin{aligned} (n_i \mathcal{F}^i)^* &= \frac{1}{2} n_i (\mathcal{F}_{\text{int}}^i + \mathcal{F}_{\text{ext}}^i) \\ &\quad - \sigma n_i \mathcal{A}^{ij} n_j (u^{\text{int}} - u^{\text{ext}}), \end{aligned} \quad (25b)$$

where "int" denotes values on the interior side of a boundary shared with another element, and "ext" denotes values on the exterior side that were sent from the neighboring element. The penalty factor σ is

$$\sigma = C \frac{(\max(p^{\text{int}}, p^{\text{ext}}) + 1)^2}{\min(h^{\text{int}}, h^{\text{ext}})}, \quad (26)$$

where p is the polynomial order perpendicular to the element boundary, and $h = 2J/J^\Sigma$ is a measure of the element size perpendicular to the element boundary. We choose the penalty parameter $C = 1.5$ in this article.

Boundary conditions are imposed through numerical fluxes as well. To impose Dirichlet-type boundary conditions $u = u_D$ on an element boundary we set

$$u^{\text{ext}} = 2u_D - u^{\text{int}}, \quad \mathcal{F}_{\text{ext}}^i = \mathcal{F}_{\text{int}}^i, \quad (27a)$$

and to impose Neumann-type boundary conditions $n_i \mathcal{F}^i = (n_i \mathcal{F}^i)_N$ we set

$$u^{\text{ext}} = u^{\text{int}}, \quad n_i \mathcal{F}_{\text{ext}}^i = 2(n_i \mathcal{F}^i)_N - n_i \mathcal{F}_{\text{int}}^i \quad (28a)$$

in the numerical fluxes, Eq. (25).

III. TEST PROBLEMS

We test the DG scheme on three problems with extremely stretched grids. All test problems are implemented in the open-source code `SpECTRE` [7] and solved with the iterative multigrid-Schwarz preconditioned Newton-Krylov elliptic solver detailed in Ref. [18].

In addition to demonstrating that the generic DG scheme can handle extremely stretched grids, we also demonstrate that we can obtain a measure of the truncation error in each element and dimension of these extremely stretched grids, which is an essential ingredient for adaptive mesh refinement (AMR). To this end we evaluate the anisotropic relative truncation error estimate detailed in Ref. [19], Eq. (57), which has been used in the `SpEC` code for a long time [20]. In logical dimension \hat{i} of an element Ω_k it is given by

$$\mathcal{T}[P_{q_i}] = \log_{10}(\max(P_1, P_2)) - \frac{\sum_{q_i=1}^{N_{k,\hat{i}}} \log_{10}(P_{q_i}) W_{q_i}}{\sum_{q_i=1}^{N_{k,\hat{i}}} W_{q_i}}, \quad (29)$$

with the exponential weights

$$W_{q_i} = \exp\left(-(q_i - N_{k,\hat{i}} + 1/2)^2\right). \quad (30)$$

Here, P_{q_i} are the "power monitors" in logical dimension \hat{i} , which are the spectral modes marginalized over the two other logical dimensions $\hat{j}, \hat{k} \neq \hat{i}$. They are given by [19]

$$P_{q_i} = \sqrt{\frac{N_{k,\hat{i}}}{N_k} \sum_{\hat{q}}^{N_k} |\tilde{u}_{\hat{q}}|^2 \delta_{\hat{q}_i q_i}}, \quad (31)$$

where the spectral modes $\tilde{u}_{\hat{q}} = \mathcal{V}_{qp}^{-1} u_p$ are obtained from the nodal data u_p using the Vandermonde matrix $\mathcal{V}_{pq} = \prod_{\hat{i}} \Phi_{q_i}(\xi_{p_i})$, and $\Phi_{q_i}(\xi)$ are the normalized Legendre polynomials. Given the relative truncation error estimate in each dimension, the p -AMR criterion increases the number of grid points in logical dimension \hat{i} of an element Ω_k , and hence the polynomial order of the expansion (10), if any tensor component of the variables u satisfies the condition

$$10^{-\mathcal{T}[P_{q_i}]} \max(|u_p|) > \mathcal{T}_{\text{target}}, \quad (32)$$

where $\mathcal{T}_{\text{target}}$ is a given target absolute truncation error. For further details see Ref. [19], Section 5.1. We show that this p -AMR criterion works well even on the extremely stretched DG grids, and that we do not need to use the compactified grid that was necessary in Ref. [4].

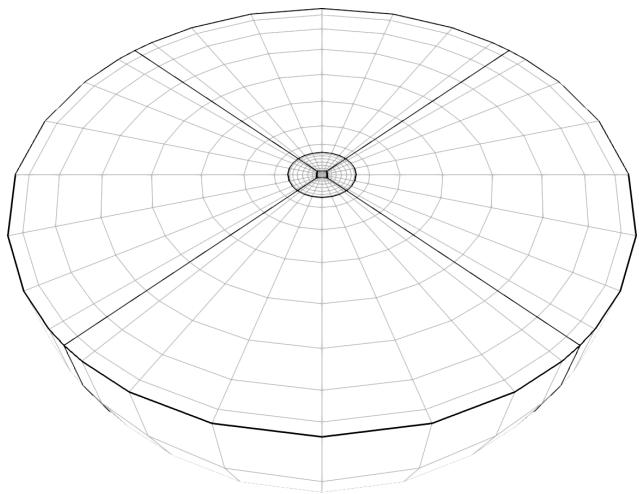


FIG. 2. Spherical domain used in the Lorentzian problem, Section III A. Two spherical shells wrap a central cube. Each shell is composed of six wedge-shaped elements (black lines) with a grid of collocation points in the element (gray lines). The inner wedges transition from a cubical inner boundary to a spherical outer boundary with a linear radial mapping. The outer wedges stretch to $R = 10^9$ with an inverse radial mapping. For this visualization, the inverse radial mapping in the outer shell is undone to be able to see both shells. Note that while the outermost circle of grid points map to $R = 10^9$ (outermost black circle), the next-to-outermost circle of grid points shown here already only map to $r = 400$ (outermost gray circle) due to the extreme grid stretching.

A. Poisson problem with Lorentzian solution

First, we test the DG scheme on a simple Poisson problem with a solution that falls off as $1/r$ at large distances. We choose the Lorentzian solution

$$u_{\text{analytic}}(\mathbf{x}) = \left(1 + r^2\right)^{-1/2}, \quad (33)$$

where $r = \sqrt{x^2 + y^2 + z^2}$ is the coordinate distance from the origin. To solve for this solution we choose the fixed source $f(\mathbf{x}) = -\nabla^2 u_{\text{analytic}}(\mathbf{x}) = 3(1 + r^2)^{-5/2}$ and solve for $u(\mathbf{x})$.

This problem was also solved in Ref. [4]. In fact, the generic weak-primal DG scheme developed here reduces to the scheme used in Ref. [4] for a flat-space Poisson equation, except for the dealiasing techniques employed in Ref. [4] that we have not found to be necessary so far, and some small differences in the definition of the penalty factor σ .

We choose a spherical domain with outer radius $R = 10^9$ and impose the solution, Eq. (33), as Dirichlet boundary conditions on the outer boundary. The domain is illustrated in Fig. 2. It consists of two spherical shells wrapped around a central cube. The spherical shells are composed of six wedges each, as pictured in Fig. 1. The wedges in the inner shell transition from a cubical inner

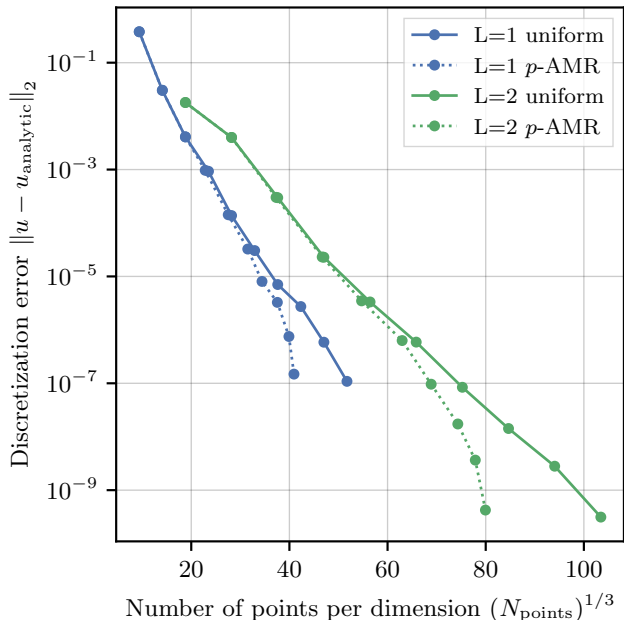


FIG. 3. Convergence of the DG scheme with increasing polynomial order P for multiple refinement levels L in the Lorentzian problem, Section III A. The error is measured as an L_2 norm over all grid points of the difference to the exact solution, Eq. (33). The error decreases exponentially with increasing polynomial order P as expected, and the p -AMR criterion is able to handle the extreme grid stretching as well.

boundary to a spherical outer boundary with a linear radial mapping, and the wedges in the outer shell employ an inverse radial mapping to stretch the grid to the outer boundary at radius 10^9 .

Fig. 3 shows that the DG scheme achieves the expected exponential convergence with increasing polynomial order P for multiple refinement levels L . The refinement levels are constructed from the domain in Fig. 2 by splitting each of the 13 elements in two along each dimension, so at $L = 1$ it has 104 elements, and at $L = 2$ it has 832 elements. At every refinement level we either increase the polynomial order in each element and dimension from $P = 1$ to $P = 10$ uniformly, or we increase the polynomial order adaptively and anisotropically using the p -AMR criterion, Eq. (32), with $\mathcal{T}_{\text{target}} = 10^{-7}$ for $L = 1$ and $\mathcal{T}_{\text{target}} = 10^{-9}$ for $L = 2$. The error converges exponentially, and the p -AMR criterion is able to handle the extreme grid stretching without the compactified grid that was necessary in Ref. [4].

B. Puncture initial data with black holes

Next, we solve a classic puncture problem for binary black hole initial data [21]. This method is widely used in the numerical relativity community to generate initial data because of its simplicity. It is characterized by the

puncture equation,

$$-\Delta u = \beta (\alpha (1 + u) + 1)^{-7}, \quad (34)$$

where Δ is the flat-space Laplacian and $u(\mathbf{x})$ is the puncture field that we solve for. The background fields $\alpha(\mathbf{x})$ and $\beta(\mathbf{x})$ are given by [22]

$$\frac{1}{\alpha} = \sum_I \frac{M_I}{2r_I}, \quad \beta = \frac{1}{8} \alpha^7 \bar{A}_{ij} \bar{A}^{ij} \quad (35a)$$

$$\bar{A}^{ij} = \frac{3}{2} \sum_I \frac{1}{r_I^2} \left(2P_I^{(i} n_I^{j)} - (\delta^{ij} - n_I^i n_I^j) P_I^k n_I^k \right. \\ \left. + \frac{4}{r_I} n_I^{(i} \epsilon^{j)kl} S_I^k n_I^l \right) \quad (35b)$$

to represent any number of black holes with masses M_I , positions \mathbf{C}_I , linear momenta \mathbf{P}_I , and spins \mathbf{S}_I . Here, $r_I = \|\mathbf{x} - \mathbf{C}_I\|$ is the Euclidean coordinate distance to the I th black hole and $\mathbf{n}_I = (\mathbf{x} - \mathbf{C}_I)/r_I$ is the radial unit normal to the I th black hole. Since the puncture equation is just a Poisson equation with a nonlinear source, it is easily represented by our generic DG scheme.

The puncture equation is an example of a problem with a non-smooth solution, which poses a challenge for spectral methods. Specifically, the puncture field is only \mathcal{C}_2 continuous at the punctures [21], so spectral methods are not expected to converge exponentially in elements that contain a puncture. Therefore, the most prominent implementation of the puncture method in the community, the `TwoPunctures` code [13], uses a special coordinate transformation to achieve rapid (but sub-exponential) convergence despite the non-smooth source. Here we achieve exponential convergence with our generic DG scheme by an hp refinement strategy, which presents an alternative and more flexible approach to the problem. We have solved a similar problem in Ref. [4] with a prototype code that was limited to Poisson-type equations.

We employ the spherical domain already used in the Lorentzian problem, Section III A, which is pictured in Fig. 2. For the puncture problem we place the outer radius at only $R = 10^5$ and employ Robin boundary conditions,

$$\partial_r(ru) = 0. \quad (36)$$

They are implemented as Neumann-type boundary conditions $(n_i \mathcal{F}^i)_N = -u/r$ in Eq. (28). We place any number of punctures on the grid to evaluate the background fields, Eq. (35). We choose the same configuration that is solved in Ref. [13], Section V, which consists of two orbiting punctures placed at $\mathbf{x}_{\pm} = (\pm 3, 0, 0)$ with masses $M_{\pm} = 0.5$, $\mathbf{P}_{\pm} = (0, \pm 0.2, 0)$, and $\mathbf{S}_{\pm} = 0$.

To demonstrate exponential convergence with our DG scheme we increase the resolution of the domain iteratively as follows: in every refinement step we split elements that contain a puncture in two in each dimension (h refinement), and increase the polynomial degree of all other elements by one in each dimension (p refinement). During this procedure we always impose a two-to-one balance at element interfaces, meaning that elements may only have

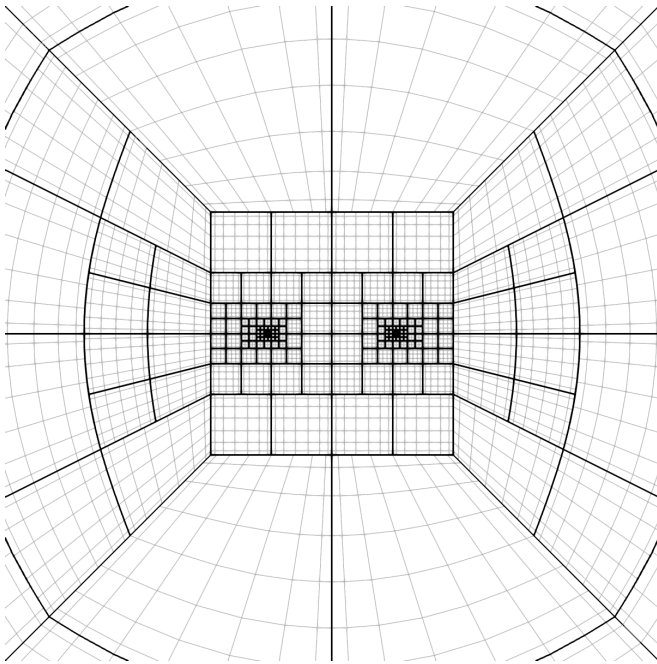


FIG. 4. Spherical domain used in the puncture problem, Section III B, after a few hp refinement steps.

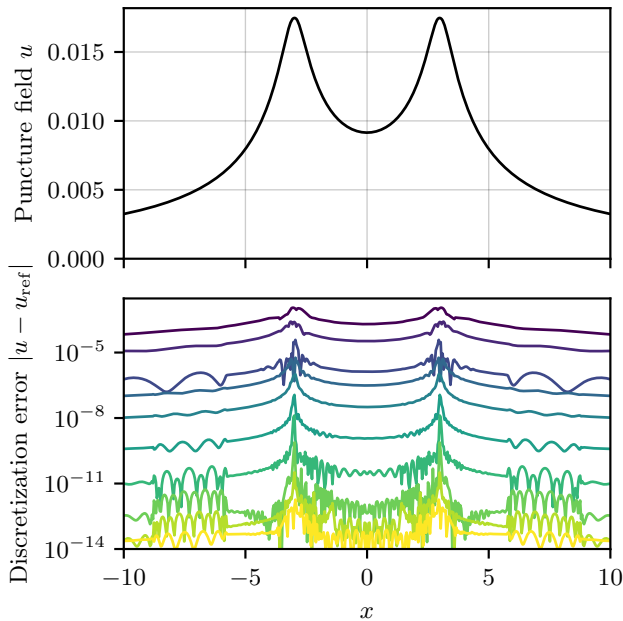


FIG. 5. *Top*: Solution to the puncture problem on the x axis at the highest resolution. *Bottom*: Numerical error of the solution at increasing resolution. The plotted error is the difference to the highest-resolution reference configuration shown in the top panel. It decreases exponentially using the hp refinement strategy detailed in Section III B. The error at the punctures is also plotted in Fig. 6.

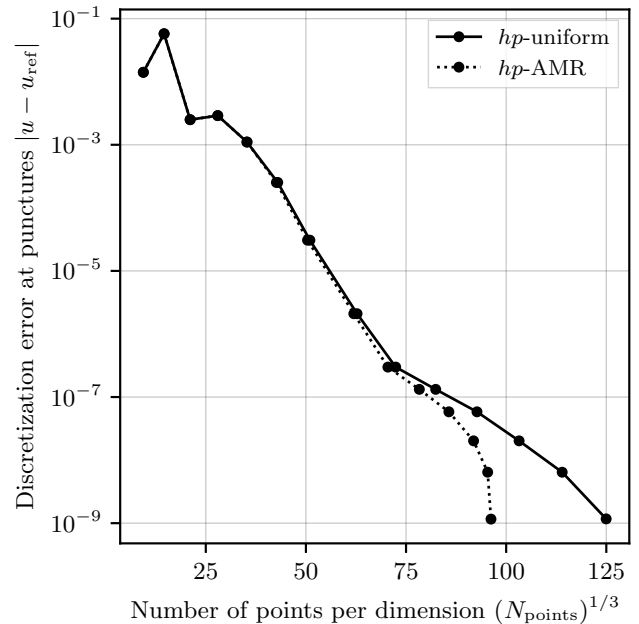


FIG. 6. Convergence of the discretization error at the position of the punctures (see Fig. 5).

two neighbors per dimension on every side. We enforce the two-to-one balance by splitting elements at interfaces where the condition is violated. This strategy leads to the domain pictured in Fig. 4 after a few refinement steps, and to the exponential convergence shown in Fig. 5. The error at the location of the punctures is also plotted in Fig. 6.

In addition to the uniform refinement strategy, we also employ the p -AMR criterion, Eq. (32), with $\mathcal{T}_{\text{target}} = 10^{-9}$ to control the polynomial degree in elements that do not contain a puncture. As in the Lorentzian problem, Section III A, we find that the p -AMR criterion performs well on the stretched grids without the compactified grid that was necessary in Ref. [4]. The full hp -AMR convergence study with the 15 refinement levels depicted in Fig. 6 (including the highest-resolution reference configuration) completed in ~ 7.5 min on one node of the CaltechHPC computing cluster at Caltech, running on 56 Intel Xeon Platinum 8276 CPU cores clocked at 2.2 GHz.

C. Binary black hole XCTS initial data

Finally, we test the DG scheme on a binary black hole initial data problem in the XCTS formulation, Eq. (5). The XCTS formulation of the Einstein constraint equations is more challenging to solve than the puncture formulation but it has several advantages. For example, it provides a way to impose a quasiequilibrium condition on the initial data by a choice of $\bar{u}_{ij} = 0$ and $\partial_t K = 0$ and then yields appropriate initial gauge choices for the evolution in form of the lapse $\alpha(\mathbf{x})$ and shift $\beta^i(\mathbf{x})$ [16].

The XCTS formulation is also equipped to generate initial data for black holes with high spins, which is difficult to achieve with the puncture method [23–25]. To this end we follow the *superposed Kerr-Schild* formalism [26] to set the conformal metric and the trace of the extrinsic curvature to the superpositions

$$\bar{\gamma}_{ij} = \delta_{ij} + \sum_{I=1}^2 e^{-r_I^2/w_I^2} (\gamma_{ij}^I - \delta_{ij}), \quad (37a)$$

$$K = \sum_{n=1}^2 e^{-r_I^2/w_I^2} K^I, \quad (37b)$$

where γ_{ij}^I and K^I are the spatial metric and the trace of the extrinsic curvature of two isolated Kerr black holes in Kerr-Schild coordinates, with r_I the Euclidean coordinate distance from either center. The superpositions are modulated by two Gaussians with widths w_I so that the influence of either of the two isolated solutions at the position of the other is strongly damped. The Gaussians also avoid logarithmic terms in the solution far away from the center where we employ the inverse radial coordinate mapping, Eq. (9c).

Orbital motion is imposed on the two black holes by a split of the shift in a *background* and an *excess* part [27],

$$\beta^i = \beta_{\text{bg}}^i + \beta_{\text{ex}}^i. \quad (38)$$

We choose the background shift

$$\beta_{\text{bg}}^i = (\mathbf{\Omega}_0 \times \mathbf{x})^i + \dot{a}_0 x^i + v_0^i, \quad (39)$$

where $\mathbf{\Omega}_0$ is the orbital angular velocity, \dot{a}_0 is a radial expansion velocity to control the eccentricity of the binary, and v_0^i is a constant velocity to control its linear momentum [26, 28]. Then, we insert Eq. (38) into the XCTS equations, Eq. (5), and henceforth solve them for β_{ex}^i instead of β^i . This split is necessary on the stretched grid to avoid numerical error in the derivatives of the shift far away from the center where $\beta_{\text{bg}}^i \propto r$. Instead, derivatives of the background shift are computed analytically. In addition, we find that it is essential on these stretched grids to solve for $\psi - 1$ and $\alpha\psi - 1$ instead of ψ and $\alpha\psi$ to avoid numerical error in the derivatives of the conformal factor and the lapse.

Given these modifications to the XCTS formulation we solve the equations on the domain illustrated in Fig. 7. The domain transitions from two excised spheres that represent the black holes to a spherical outer boundary at radius R . At the two excision surfaces in the interior of the domain we impose apparent-horizon boundary conditions [29] with an optional negative expansion [30],

$$n^k \bar{\nabla}_k \psi = \frac{\psi^3}{8\alpha} n_i n_j \left((\bar{L}\beta)^{ij} - \bar{u}^{ij} \right) \quad (40a)$$

$$\begin{aligned} & - \frac{\psi}{4} \bar{m}^{ij} \bar{\nabla}_i n_j - \frac{1}{6} K \psi^3 - \frac{\psi^3}{4} \Theta_I, \\ \beta^i &= - \frac{\alpha}{\psi^2} n^i + (\mathbf{\Omega}_r^I \times (\mathbf{x} - \mathbf{x}_I))^i \quad (40b) \\ & + n^i \psi^{-2} (n_j \beta_I^j + \alpha_I), \end{aligned}$$

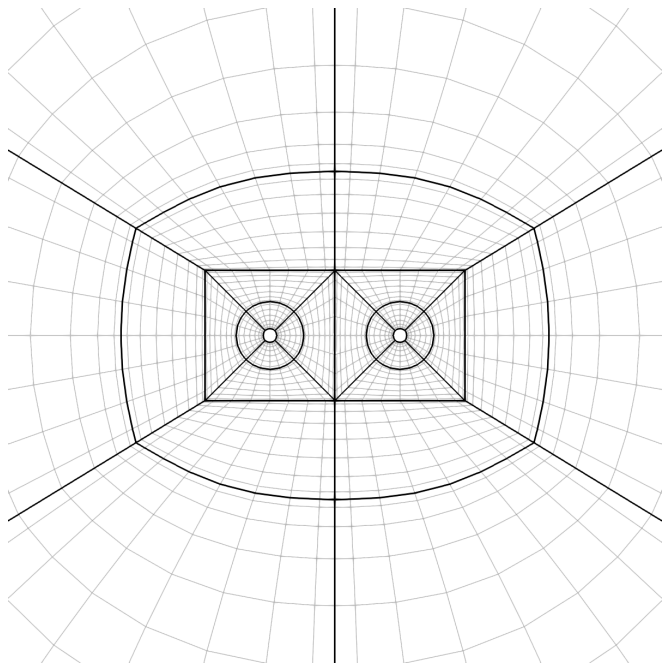


FIG. 7. Binary black hole domain used in the XCTS initial data problem, Section III C. The domain transitions from two excised spheres, to two cubes, to an enveloping sphere, all the way to a spherical outer boundary at $R = 10^9$ (not shown). The enveloping sphere is split in half once in radial direction (outermost black ellipse), and the outer sphere is split in half twice in radial direction (not shown), so the domain has 84 elements in total.

where n^i is the unit normal to the excision surface pointing out of the computational domain towards the center \mathbf{x}_I of the excision, $\bar{m}^{ij} = \bar{\gamma}_{ij} - n_i n_j$ is the conformal surface metric, and $\mathbf{\Omega}_r^I$ are the rotation parameters that induce spin on the black hole. The expansion Θ_I can be set to zero to impose that the excision surface is an apparent horizon, or to a negative value obtained by evaluating the isolated Kerr solution at the location of the excision surface [30]. The last term in Eq. (40b) also corresponds to the negative-expansion boundary conditions and is obtained by evaluating the lapse $\alpha_I(\mathbf{x})$ and shift $\beta_I^j(\mathbf{x})$ of the isolated Kerr solution [30]. In addition to Eq. (40) we impose the lapse of the isolated Kerr solution as Dirichlet boundary condition on the excision surface.¹

At the outer boundary we impose one of two types of boundary conditions. First, we impose standard asymptotically flat Dirichlet boundary conditions,

$$\psi = 1, \quad \alpha\psi = 1, \quad \beta_{\text{ex}}^i = 0. \quad (41)$$

Second, we impose new Robin boundary conditions,

$$\partial_r(r\psi) = 0, \quad \partial_r(r\alpha\psi) = 0, \quad \partial_r(r\beta_{\text{ex}}^i) = 0. \quad (42)$$

¹ Note that the SpEC code typically imposes the *superposed* lapse on the excision surfaces [30], rather than the lapse of the isolated Kerr solutions.

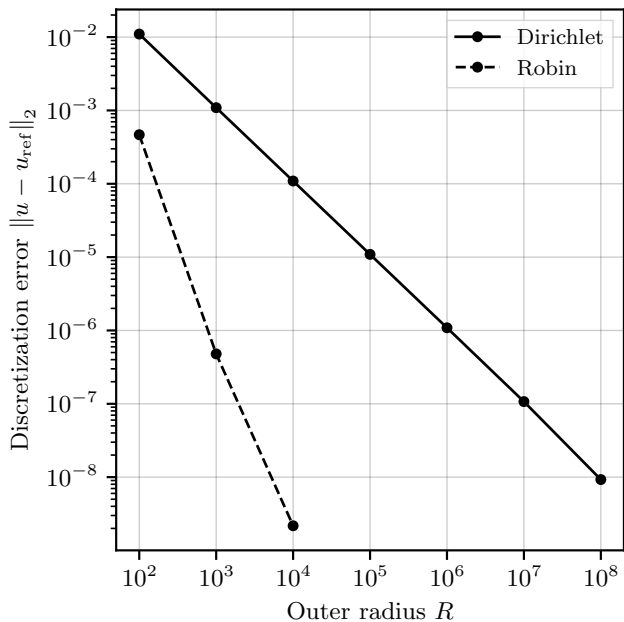


FIG. 8. Error incurred by the Dirichlet and Robin outer boundary conditions in the XCTS problem, Section III C, with increasing radius of the outer boundary R . The Dirichlet boundary conditions incur an error of order $\mathcal{O}(1/R)$, whereas the Robin boundary conditions incur an error of order $\mathcal{O}(1/R^2)$, thus allowing to place the outer boundary closer to the center.

Robin-type boundary conditions for the Einstein constraints have been proposed as early as Refs. [31, 32], but not for the more modern XCTS formulation. The Robin boundary conditions on ψ and $\alpha\psi$ are straightforwardly implemented as Neumann-type conditions on the fluxes in Eq. (28), $(n_i \bar{\nabla}^i \psi)_N = -\psi/r$ and $(n_i \bar{\nabla}^i \alpha\psi)_N = -\alpha\psi/r$. To implement the Robin boundary condition for β_{ex}^i we recast it as a Neumann-type condition on the flux $n_i \mathcal{F}_{\beta_{\text{ex}}}^i = n_i (\bar{L}\beta_{\text{ex}})^{ij}$ as well. To this end, we define the projection operator $P_j^i = \delta_j^i - n^i n_j$ to set the normal component of the shift gradient,

$$(\bar{\nabla}_i \beta_{\text{ex}}^j)_N = P_i^k \bar{\nabla}_k \beta_{\text{ex}}^j - n_i \frac{\beta_{\text{ex}}^j}{r}, \quad (43)$$

and then apply the longitudinal operator, Eq. (6), to obtain

$$(n_i (\bar{L}\beta_{\text{ex}})^{ij})_N = n_i (\bar{L}\beta_{\text{ex}})^{ij} - \left[\frac{\beta_{\text{ex}}^j}{r} + n^k \bar{\nabla}_k \beta_{\text{ex}}^j \right] - \frac{1}{3} n^j n_i \left[\frac{\beta_{\text{ex}}^i}{r} + n^k \bar{\nabla}_k \beta_{\text{ex}}^i \right] \quad (44)$$

We have assumed conformal flatness at the outer boundary in this derivation, which is given approximately by the superposition in Eq. (37).

We solve for an equal-mass and nonspinning black hole binary in this article. Our implementation also supports unequal masses and spins, but neither is particularly

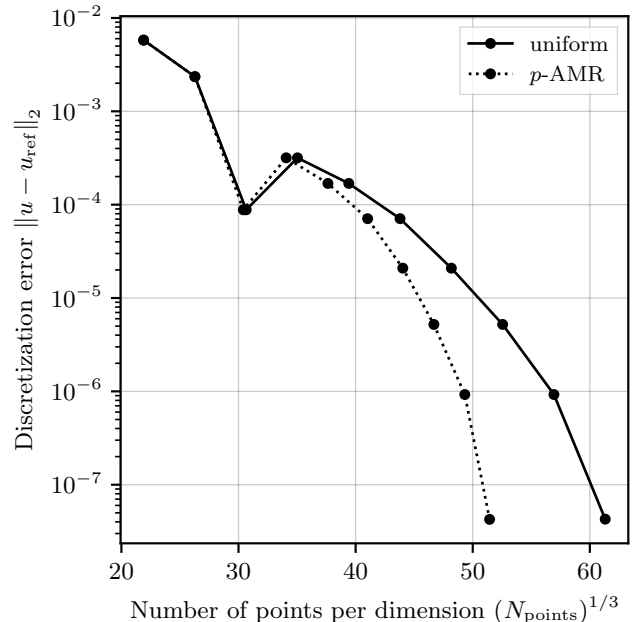


FIG. 9. Convergence of the DG scheme for the XCTS problem, Section III C.

relevant to test the extremely stretched grids and outer boundary conditions. All parameters are listed in the supplementary material. We compute a discretization error $\|u - u_{\text{ref}}\|_2$ by interpolating the variables $u_\alpha = \{\psi, \alpha\psi, \beta_{\text{ex}}^i\}$ to three sample points in the domain, $\mathbf{x}_1 = (0, 0, 0)$, $\mathbf{x}_2 = (8.7, 0, 0)$, and $\mathbf{x}_3 = (100, 0, 0)$, taking the difference to a high-resolution reference simulation, and then taking the L_2 norm over all variables and sample points.

Figure 8 compares the two types of boundary conditions at the outer boundary. As expected, the error incurred by the Dirichlet boundary conditions is of order $\mathcal{O}(1/R)$, whereas the error incurred by the Robin boundary conditions is of order $\mathcal{O}(1/R^2)$. Therefore, in the following we place the outer boundary at $R = 10^9$ when using Dirichlet boundary conditions, and at $R = 10^5$ when using Robin boundary conditions.

Figure 9 shows the convergence of the DG scheme for the XCTS problem with increasing polynomial order in each element. We either increase the polynomial order in all elements uniformly by one in each dimension (solid line), or apply the p -AMR criterion, Eq. (32), with $\mathcal{T}_{\text{target}} = 10^{-8}$ (dotted line). The discretization error decreases exponentially on the extremely stretched grids, and the p -AMR criterion is able to handle the extreme grid stretching as well.

The convergence for Dirichlet and Robin boundary conditions in Fig. 9 is identical. However, the smaller outer radius for the Robin boundary conditions improves the convergence rate of the elliptic solver, reducing its time to solution by about 30%. The full p -AMR convergence study with the 10 refinement levels depicted in Fig. 9

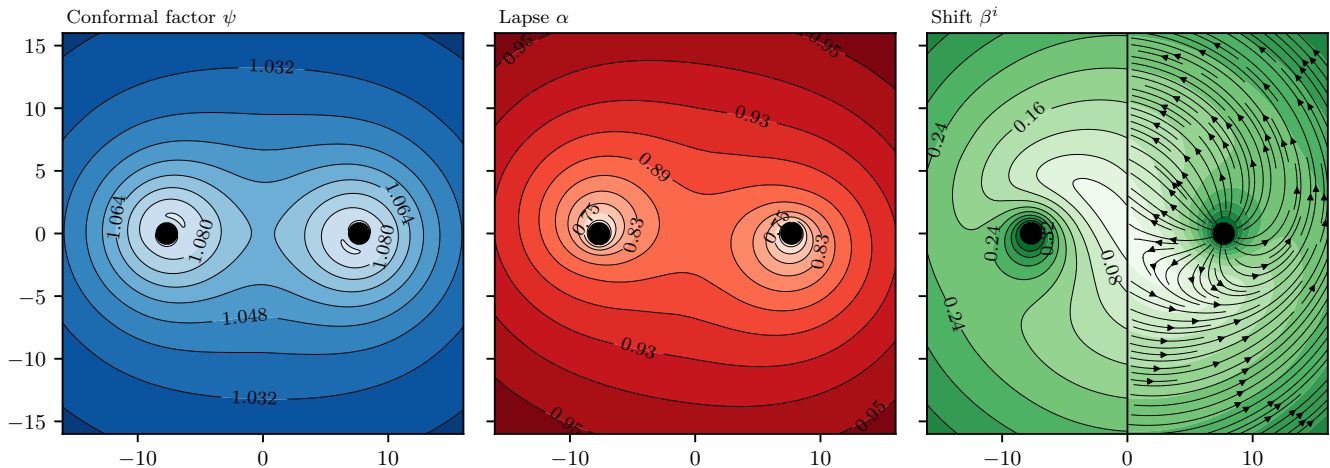


FIG. 10. Solution to the binary black hole initial data problem in the XCTS formulation, Section III C.

completed in ~ 10 min on one node of the CaltechHPC computing cluster at Caltech, running on 56 Intel Xeon Platinum 8276 CPU cores clocked at 2.2 GHz. Fig. 10 shows the solution to the XCTS problem at the highest resolution.

IV. CONCLUSION

We have developed a generic discontinuous Galerkin (DG) scheme that is able to handle extremely stretched grids for initial data problems in numerical relativity. Important ingredients for the DG scheme to handle the extreme grid stretching are: a primal DG formulation, the weak form of the DG residuals, the use of Legendre-Gauss-Lobatto (LGL) over Legendre-Gauss (LG) collocation points, and the choice to solve for $\psi - 1$ and $\alpha\psi - 1$ instead of ψ and $\alpha\psi$ for the XCTS equations.

With these ingredients we have demonstrated exponential convergence of the DG scheme for three test problems with Jacobians as large as $J \sim 10^{35}$: a Poisson problem with a Lorentzian solution, a puncture problem for binary black hole initial data, and a binary black hole initial data problem in the XCTS formulation. The scheme achieves exponential convergence with increasing polynomial order and is able to handle anisotropic adaptive mesh refinement (AMR) without the compactified grid that was necessary in Ref. [4].

The generic weak-primal DG scheme is implemented in the open-source numerical relativity code SpECTRE [7] and solves the test problems with the iterative multigrid-Schwarz preconditioned Newton-Krylov elliptic solver detailed in Ref. [18]. The new DG scheme is significantly simpler to extend to new elliptic equations than the formulation used in Ref. [5], since the concept of auxiliary variables is avoided altogether. The results in this article are reproducible with the input files provided in the supplementary material.

Using the DG scheme we are able to solve the puncture problem for binary black hole initial data with exponential convergence, which is a challenging problem for spectral methods due to its non-smooth solution. Our approach provides a more flexible alternative to apply spectral methods to the puncture problem than the special coordinate transformation used in the TwoPunctures code [13]. For example, we are able to handle randomly placed punctures on the computational grid with no special treatment in our code.

Most importantly, with the DG scheme laid out in this article we are able to produce binary black hole initial data in the XCTS formulation extending to distances of 10^9 with a DG method for the first time. We also propose new Robin boundary conditions for the XCTS equations that allow us to place the outer boundary at only 10^5 , alleviating some of the grid stretching. These advancements now allow us to generate high-quality conformally-curved initial data for our numerical relativity simulations of binary black holes with the SpECTRE code. The DG method allows us to parallelize the initial data solver on computing clusters, as detailed in Ref. [18], so typical configurations solve in a few minutes on a single node of a computing cluster. In addition to the equal-mass and nonspinning configuration solved in this article we are able to generate initial data with unequal masses and high spins in the superposed Kerr-Schild (SXS) formalism, as well as variations such as superposed Harmonic Kerr (SHK) or spherical Kerr-Schild initial data. We also support negative-expansion boundary conditions [30]. Forthcoming work on the SpECTRE initial data solver for binary black holes will focus on control loops for the initial data parameters in the spirit of Ref. [28].

The results presented in this article are also an important step to support forthcoming work on initial data in theories beyond general relativity [33], as well as initial data involving neutron stars. They lay the foundation for high-quality initial data in the SpECTRE code to be used

in the next generation of numerical relativity simulations. Due to the open source nature of the `SpECTRE` code, the initial data solver is also publicly available to the numerical relativity community and the generated initial data can be imported into other codes as well.²

ACKNOWLEDGMENTS

NV thanks Harald Pfeiffer and Saul Teukolsky for helpful discussions, as well as Larry Kidder, Guillermo Lara, and the `SpECTRE` development team for the collaborative work that enabled this research. Computations were performed with the `SpECTRE` code [7] on the CaltechHPC cluster at Caltech. The figures in this article were produced with `matplotlib` [34, 35], `TikZ` [36], and `ParaView` [37]. This work was supported in part by the Sherman Fairchild Foundation and by NSF Grants No. PHY-2011961, No. PHY-2011968, and No. OAC-1931266.

Appendix A: Fluxes and sources for the XCTS equations

The XCTS equations, Eq. (5), can be written in first-order flux form, Eq. (1). For the Hamiltonian constraint,

Eq. (5a), the fluxes and sources are

$$\mathcal{F}_\psi^i = \bar{\gamma}^{ij} \partial_j \psi, \quad (\text{A1a})$$

$$\begin{aligned} \mathcal{S}_\psi = & -\bar{\Gamma}_{ij}^i \mathcal{F}_\psi^j + \frac{1}{8} \psi \bar{R} + \frac{1}{12} \psi^5 K^2 \\ & - \frac{1}{8} \psi^{-7} \bar{A}^2 - 2\pi \psi^5 \rho, \end{aligned} \quad (\text{A1b})$$

and for the momentum constraint, Eq. (5c), the fluxes and sources are

$$\mathcal{F}_\beta^{ij} = (\bar{L}\beta)^{ij} = \bar{\nabla}^i \beta^j + \bar{\nabla}^j \beta^i - \frac{2}{3} \bar{\gamma}^{ij} \bar{\nabla}_k \beta^k, \quad (\text{A1e})$$

$$\begin{aligned} \mathcal{S}_\beta^i = & -\bar{\Gamma}_{jk}^j \mathcal{F}_\beta^{ik} - \bar{\Gamma}_{jk}^i \mathcal{F}_\beta^{jk} \\ & + \frac{2\alpha\psi}{\psi^7} \bar{A}^{ij} \left(\frac{\partial_j(\alpha\psi)}{\alpha\psi} - 7 \frac{\partial_j\psi}{\psi} \right) \\ & - \bar{D}_j \left((\bar{L}\beta_{\text{bg}})^{ij} - \bar{u}^{ij} \right) \\ & + \frac{4}{3} \frac{\alpha\psi}{\psi} \bar{D}^i K + 16\pi (\alpha\psi) \psi^3 S^i, \end{aligned} \quad (\text{A1f})$$

where

$$\bar{A}^{ij} = \frac{\psi^7}{2\alpha\psi} \left((\bar{L}\beta)^{ij} + (\bar{L}\beta_{\text{bg}})^{ij} - \bar{u}^{ij} \right) \quad (\text{A1g})$$

and all $f_\alpha = 0$.

for the lapse equation, Eq. (5b), the fluxes and sources are

$$\mathcal{F}_{(\alpha\psi)}^i = \bar{\gamma}^{ij} \partial_j \alpha \psi, \quad (\text{A1c})$$

$$\begin{aligned} \mathcal{S}_{(\alpha\psi)} = & -\bar{\Gamma}_{ij}^i \mathcal{F}_{(\alpha\psi)}^j + \alpha \psi \left(\frac{7}{8} \psi^{-8} \bar{A}^2 + \frac{5}{12} \psi^4 K^2 \right. \\ & \left. + \frac{1}{8} \bar{R} + 2\pi \psi^4 (\rho + 2S) \right) - \psi^5 \partial_t K \\ & + \psi^5 \left(\beta^i \bar{D}_i K + \beta_{\text{bg}}^i \bar{D}_i K \right), \end{aligned} \quad (\text{A1d})$$

² Instructions are provided on <https://spectre-code.org> and on request from the author.

-
- [1] D. Arnold, F. Brezzi, B. Cockburn, and D. L. Marini, Unified analysis of discontinuous Galerkin methods for elliptic problems, *SIAM Journal on Numerical Analysis* **39**, 1749 (2002).
 - [2] M. F. Wheeler, An elliptic Collocation-Finite element method with interior penalties, *SIAM J. Numer. Anal.* **15**, 152 (1978).
 - [3] D. Schötzau, C. Schwab, T. Wihler, and M. Wirz, Exponential convergence of hp-DGFEM for elliptic problems in polyhedral domains, in *Spectral and High Order Methods for Partial Differential Equations - ICOSAHOM 2012* (Springer International Publishing, 2014) pp. 57–73.
 - [4] T. Vincent, H. P. Pfeiffer, and N. L. Fischer, hp-adaptive discontinuous Galerkin solver for elliptic equations in numerical relativity, *Phys. Rev. D* **100**, 084052 (2019), [arXiv:1907.01572](https://arxiv.org/abs/1907.01572) [physics.comp-ph].
 - [5] N. L. Fischer and H. P. Pfeiffer, Unified discontinuous Galerkin scheme for a large class of elliptic equations, *Phys. Rev. D* **105**, 024034 (2022), [arXiv:2108.05826](https://arxiv.org/abs/2108.05826) [math.NA].
 - [6] H. P. Pfeiffer, L. E. Kidder, M. A. Scheel, and S. A. Teukolsky, A multidomain spectral method for solving elliptic equations, *Comput. Phys. Commun.* **152**, 253 (2003).
 - [7] N. Deppe, W. Throwe, L. E. Kidder, N. L. Vu, K. C. Nelli, C. Armaza, M. S. Bonilla, F. Hébert, Y. Kim, P. Kumar, G. Lovelace, A. Macedo, J. Moxon, E. O’Shea, H. P. Pfeiffer, M. A. Scheel, S. A. Teukolsky, N. A. Wittek, *et al.*, *SpECTRE v2024.04.12*, [10.5281/zenodo.10967177](https://zenodo.org/record/10967177) (2024).
 - [8] E.ourgoulhon, P. Grandclément, J.-A. Marck, J. Novak, and K. Taniguchi, *LORENE*, <http://www.lorene.obspm.fr>.
 - [9] P. Grandclément, Accurate and realistic initial data for black hole-neutron star binaries, *Phys. Rev. D* **74**, 124002 (2006), [arXiv:gr-qc/0609044](https://arxiv.org/abs/gr-qc/0609044).
 - [10] P. Grandclément, KADATH: A spectral solver for theoretical physics, *J. Comput. Phys.* **229**, 3334 (2010).

- [11] L. J. Papenfort, S. D. Tootle, P. Grandclément, E. R. Most, and L. Rezzolla, New public code for initial data of unequal-mass, spinning compact-object binaries, *Phys. Rev. D* **104**, 024057 (2021), [arXiv:2103.09911 \[gr-qc\]](#).
- [12] W. Tichy, A new numerical method to construct binary neutron star initial data, *Class. Quant. Grav.* **26**, 175018 (2009), [arXiv:0908.0620 \[gr-qc\]](#).
- [13] M. Ansorg, B. Bruegmann, and W. Tichy, A single-domain spectral method for black hole puncture data, *Phys. Rev. D* **70**, 064011 (2004), [arXiv:gr-qc/0404056](#).
- [14] J. W. York, Jr., Conformal ‘thin sandwich’ data for the initial-value problem of general relativity, *Phys. Rev. Lett.* **82**, 1350 (1999), [arXiv:gr-qc/9810051](#).
- [15] H. P. Pfeiffer and J. W. York, Jr., Extrinsic curvature and the Einstein constraints, *Phys. Rev. D* **67**, 044022 (2003), [arXiv:gr-qc/0207095](#).
- [16] H. P. Pfeiffer, The initial value problem in numerical relativity, *J. Hyperbolic Differ. Equ.* **2**, 497 (2005), [arXiv:gr-qc/0412002](#).
- [17] N. L. Vu, S. Rodriguez, T. Włodarczyk, G. Lovelace, H. P. Pfeiffer, G. S. Bonilla, N. Deppe, F. Hébert, L. E. Kidder, J. Moxon, and W. Throwe, High-accuracy numerical models of brownian thermal noise in thin mirror coatings, [arXiv:2111.06893 \[astro-ph.IM\]](#) (2021).
- [18] N. L. Vu, H. P. Pfeiffer, G. S. Bonilla, N. Deppe, F. Hébert, L. E. Kidder, G. Lovelace, J. Moxon, M. A. Scheel, S. A. Teukolsky, W. Throwe, N. A. Wittek, and T. Włodarczyk, A scalable elliptic solver with task-based parallelism for the SpECTRE code, *Phys. Rev. D* **105**, 084027 (2022), [arXiv:2111.06767 \[gr-qc\]](#).
- [19] B. Szilágyi, Key elements of robustness in binary black hole evolutions using spectral methods, *Int. J. Mod. Phys. D* **23**, 1430014 (2014), [arXiv:1405.3693 \[gr-qc\]](#).
- [20] M. Boyle *et al.* (SXS), The SXS collaboration catalog of binary black hole simulations, *Classical and Quantum Gravity* **36**, 195006 (2019), [arXiv:1904.04831 \[gr-qc\]](#).
- [21] S. Brandt and B. Brügmann, A simple construction of initial data for multiple black holes, *Phys. Rev. Lett.* **78**, 3606 (1997), [arXiv:gr-qc/9703066](#).
- [22] J. M. Bowen and J. W. York, Jr., Time asymmetric initial data for black holes and black hole collisions, *Phys. Rev. D* **21**, 2047 (1980).
- [23] S. Dain, C. O. Lousto, and Y. Zlochower, Extra-large remnant recoil velocities and spins from near-extremal-Bowen-York-spin black-hole binaries, *Phys. Rev. D* **78**, 024039 (2008), [arXiv:0803.0351 \[gr-qc\]](#).
- [24] S. Dain, C. O. Lousto, and R. Takahashi, New conformally flat initial data for spinning black holes, *Phys. Rev. D* **65**, 104038 (2002), [arXiv:gr-qc/0201062](#).
- [25] I. Ruchlin, J. Healy, C. O. Lousto, and Y. Zlochower, Puncture initial data for black-hole binaries with high spins and high boosts, *Phys. Rev. D* **95**, 024033 (2017), [arXiv:1410.8607 \[gr-qc\]](#).
- [26] G. Lovelace, R. Owen, H. P. Pfeiffer, and T. Chu, Binary-black-hole initial data with nearly-extremal spins, *Phys. Rev. D* **78**, 084017 (2008), [arXiv:0805.4192 \[gr-qc\]](#).
- [27] H. P. Pfeiffer, *Initial Data for Black Hole Evolutions*, Ph.D. thesis, Cornell University (2003), [arXiv:gr-qc/0510016 \[gr-qc\]](#).
- [28] S. Ossokine, F. Foucart, H. P. Pfeiffer, M. Boyle, and B. Szilágyi, Improvements to the construction of binary black hole initial data, *Class. Quantum Gravity* **32**, 245010 (2015), [arXiv:1506.01689 \[gr-qc\]](#).
- [29] G. B. Cook and H. P. Pfeiffer, Excision boundary conditions for black hole initial data, *Phys. Rev. D* **70**, 104016 (2004), [arXiv:gr-qc/0407078](#).
- [30] V. Varma, M. A. Scheel, and H. P. Pfeiffer, Comparison of binary black hole initial data sets, *Phys. Rev. D* **98**, 104011 (2018), [arXiv:1808.08228 \[gr-qc\]](#).
- [31] G. B. Cook, M. W. Choptuik, M. R. Dubal, S. Klasky, R. A. Matzner, and S. R. Oliveira, Three-dimensional initial data for the collision of two black holes, *Phys. Rev. D* **47**, 1471 (1993).
- [32] G. B. Cook, Initial data for axisymmetric black-hole collisions, *Phys. Rev. D* **44**, 2983 (1991).
- [33] P. J. Nee, G. Lara, H. P. Pfeiffer, and N. L. Vu, Quasistationary hair for binary black hole systems in scalar Gauss-Bonnet gravity, in preparation (2024).
- [34] J. D. Hunter, Matplotlib: A 2d graphics environment, *Comput. Sci. Eng.* **9**, 90 (2007).
- [35] T. A. Caswell *et al.*, [matplotlib v3.3.3](#), 10.5281/zenodo.4268928 (2020).
- [36] T. Tantau, [pgf - a portable graphic format for TeX](#), [github:pgf-tikz/pgf](#) (2021).
- [37] J. Ahrens, B. Geveci, and C. Law, ParaView: An end-user tool for large-data visualization, in *Visualization Handbook* (Butterworth-Heinemann, Burlington, 2005).